Supplementary Information for

Perfect crystals grown from imperfect interfaces

Claudiu V. Falub[1,*,#], Mojmír Meduňa[2,3,#], Daniel Chrastina[4], Fabio Isa[4], Anna Marzegalli[5], Thomas Kreiliger[1], Alfonso G. Taboada[1], Giovanni Isella[4], Leo Miglio[5], Alex Dommann[6] & Hans von Känel[1]

[1]*Laboratory for Solid State Physics, ETH-Zürich, Schafmattstrasse 16, 8093 Zürich, Switzerland*
[2]*Department of Condensed Matter Physics, Masaryk University, Kotlářská 2, 61137 Brno, Czech Republic*
[3]*CEITEC, Masaryk University, Kamenice 5, 60177 Brno, Czech Republic*
[4]*L-NESS, Department of Physics, Politecnico di Milano, via Anzani 42, 22100 Como, Italy*
[5]*L-NESS, Department of Materials Science, Università di Milano-Bicocca, via Cozzi 53, 20126 Milano, Italy*
[6]*Centre Suisse d'Electronique et Microtechnique, Jaquet-Droz 1, 2002 Neuchatel, Switzerland*

Correspondence and requests for materials should be addressed to C.V.F. (cfalub@phys.ethz.ch)

[*] Present address: OC Oerlikon Advanced Technologies, Iramali 18, 9496 Balzers, Liechtenstein
[#] These authors contributed equally to this work.

Supplementary methods

S1. Sample preparation

The 4" (001)-oriented (within ± 0.5°) Si substrates were patterned into arrays of uniformly spaced Si pillars by conventional photolithography and deep reactive ion etching (DRIE), as shown in Fig. S1. Silicon pillars with height h = 8 μm, base width w = 2 μm and spacing d = 1 to 4 μm were used in this work. Prior to deposition, the patterned Si substrates were cleaned using the industry standard RCA method, and the native oxide was removed by a 5% HF dip and subsequent rinse in ultrapure water.

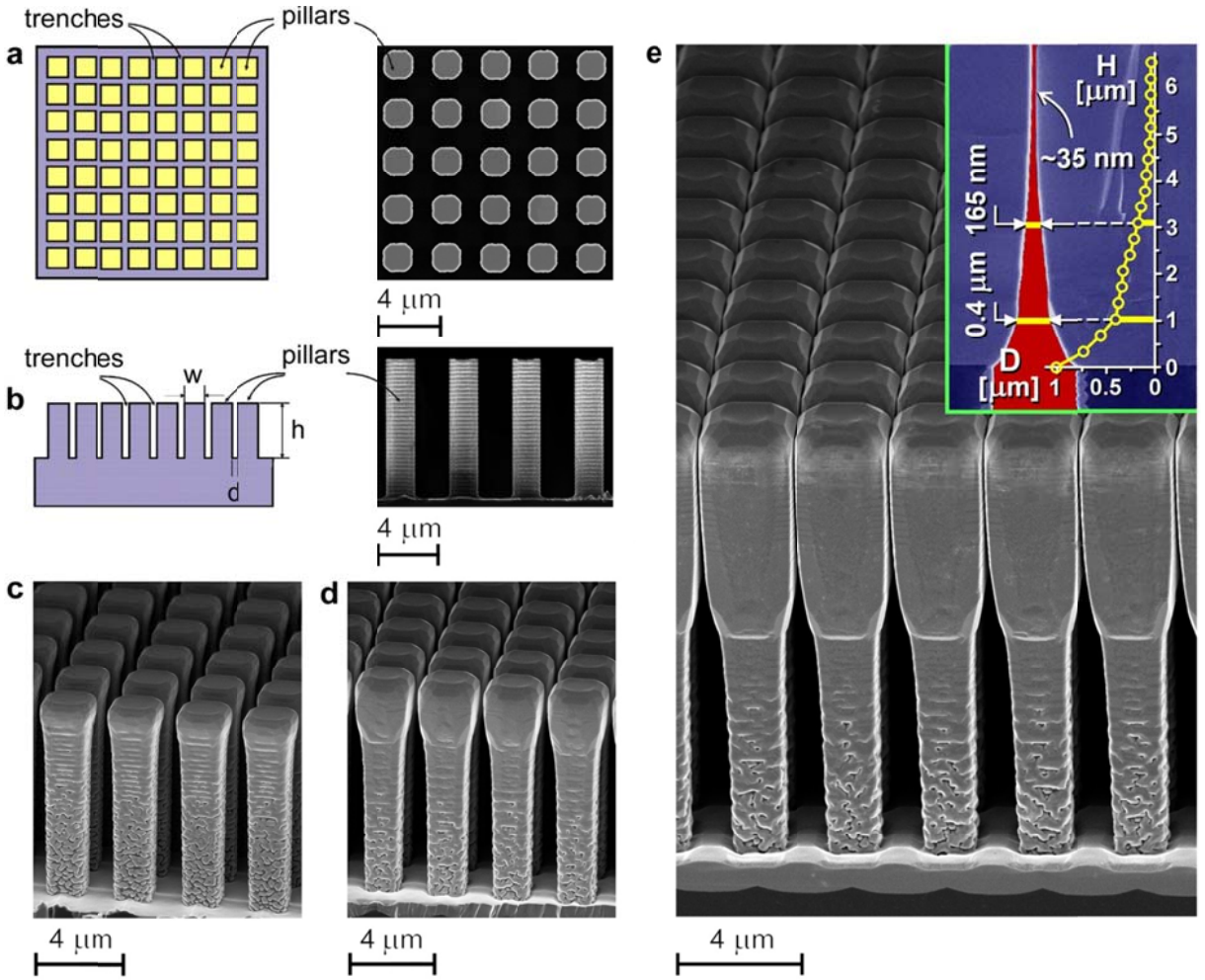

Figure S1 | Space filling arrays of Ge crystals. Schematic and SEM micrographs of Si pillar arrays (height h, base width w and spacing d) are fabricated from Si(001) substrates by photolithography and deep reactive ion etching: **a**, top-view; **b**, side-view. SEM micrographs in perspective view of 1.2-μm (**c**), 3.1-μm (**d**), and 7.3-μm (**e**) tall Ge crystals grown on patterned Si wafers with 8-μm-tall and 2-μm-wide Si pillars, spaced by 1 μm. The inset in (e) shows a graph of the distance, D, between two adjacent crystals as a function of the crystal height superimposed onto a coloured cross-section SEM micrograph, revealing the self-limited lateral growth.

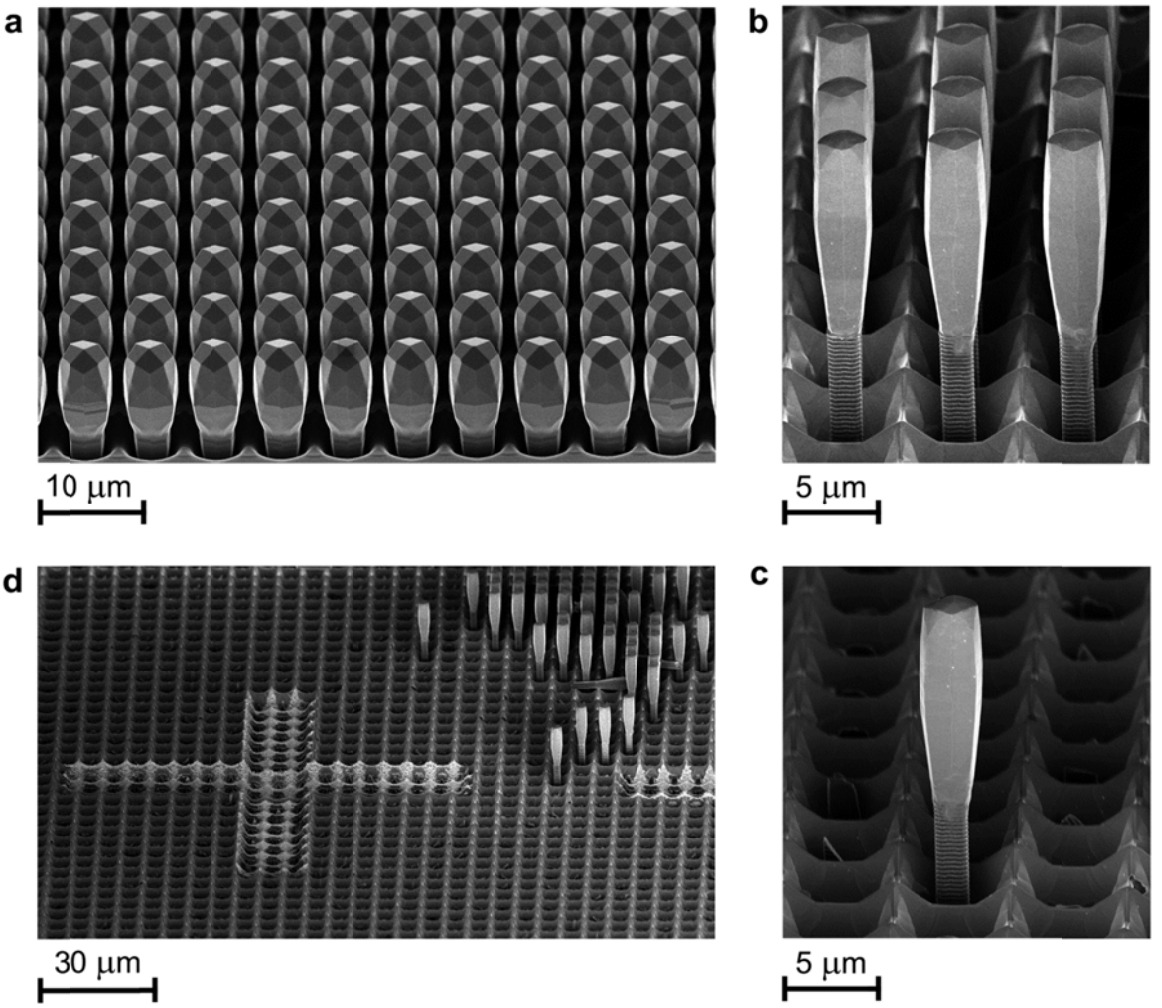

Figure S2 | Preparation of isolated Ge crystals. SEM micrographs in perspective view of 11-µm-tall Ge crystals with inclined top facets grown on patterned Si wafers with 8-µm-tall and 2-µm-wide Si pillars, spaced by 4 µm: **a**, as grown; **b**, after etching in H_2O_2 solution; **c**, neighbouring Ge crystals are removed by using micromanipulators; **d**, some reference marks in the vicinity of the isolated Ge crystals were written with a focused ion beam (FIB).

Once loaded into the growth chamber, substrates were outgassed in UHV for 15 min at 300°C before ramping to the growth temperature. Subsequently, Ge crystals were grown by low-energy plasma-enhanced chemical vapour deposition (LEPECVD)[36] at a rate of ~ 4 nm/s and at a temperature 490°C using germane (GeH_4) as a reactive gas[27]. The base pressure in the growth chamber was below 1×10^{-9} mbar; during growth the pressure was ~ 2×10^{-2} mbar. Samples with isolated Ge crystals were fabricated by etching the dense arrays in 30 wt% H_2O_2 solution (90 seconds at 70°C) and by removing neighbouring crystals using micromanipulators inside a scanning electron microscope (Fig. S2 and Supplementary Movie S5). Reference marks in the vicinity of the isolated Ge crystals used for nanodiffraction experiments were written with a focused ion beam (FIB), so that these crystals could be located using the optical microscope attached to the diffractometer stage.

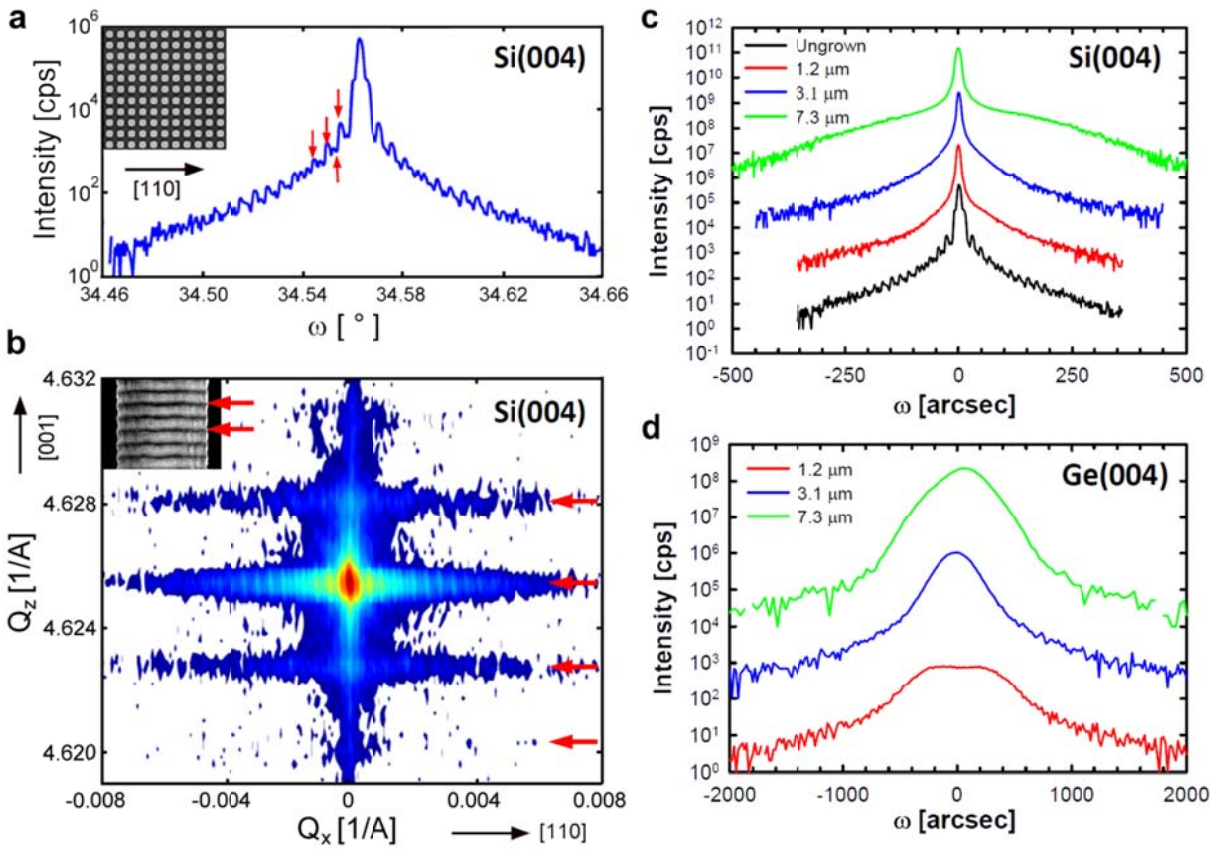

Figure S3 | a, ω scan around the Si(004) Bragg peak for the Si pillar array of Fig. S1a, exhibiting modulation (indicated by red arrows) due to the periodic arrangement of Si pillars. **b**, RSM measured around Si(004) reflection for the same sample. Besides the modulation along the Q_x direction there is also a modulation along Q_z (red arrows) due to the ripples formed during the DRIE process. **c**, **d**, Comparison between ω scans around Si and Ge(004) reflections before and after Ge growth. The curves are displaced in the vertical direction for clarity.

S2. Laboratory high-resolution X-ray diffraction

Prior to the synchrotron nanodiffraction experiments, conventional high-resolution X-ray diffraction (XRD) was used to investigate the crystalline quality and strain of the Ge crystals. The high-resolution XRD measurements, e.g. ω and θ–2θ scans, and reciprocal space maps (RSMs), were performed with Cu Kα_1 radiation using a PANalytical X'Pert Pro-MRD diffractometer equipped with a 4-bounce Ge(220) crystal monochromator on the incident beam and an analyser crystal and a Xe point detector on the diffracted beam. The X-ray beam diameter on the sample was ~ 1 mm. Therefore, depending on the lateral pattern dimensions, several thousand Ge crystals were probed simultaneously. Prior to the Ge deposition, the uniformly spaced Si pillars (periodicity along [110] direction of ~ 2.9 μm from SEM measurements) produce a diffraction pattern with periodicity along the Q_x direction $d_{[110]} = \lambda/(2\Delta\omega_x \sin\theta) \sim 3.01$ μm, where λ is the wavelength of the X-rays, θ the incidence angle, and $\Delta\omega_x$ is the angle between two adjacent satellite peaks along the Q_x direction (Fig. S3a, b)[37].

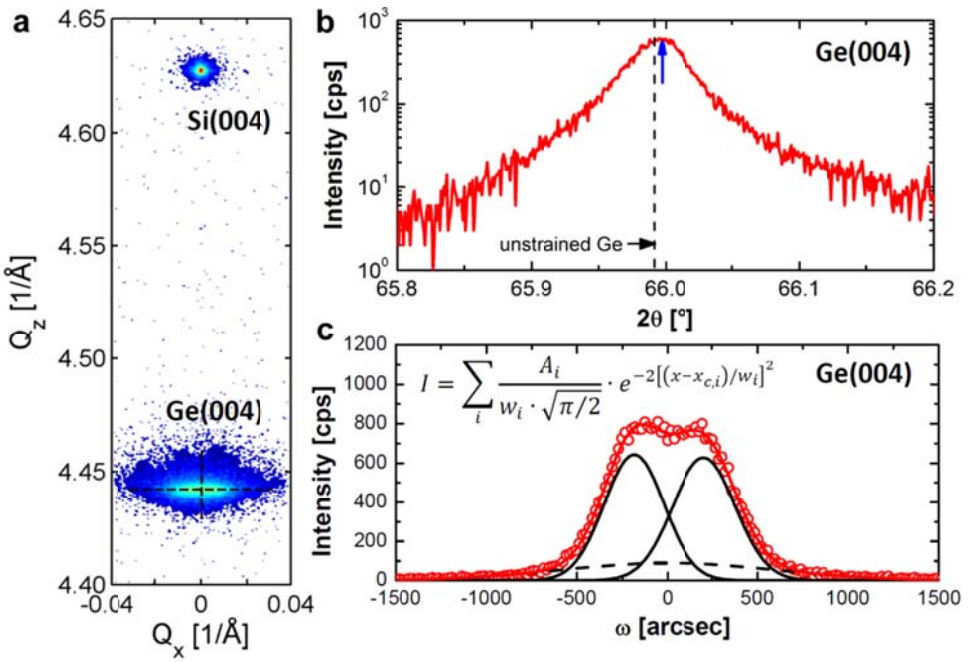

Figure S4 | a, RSM measured around the Si(004) and Ge(004) Bragg peaks for the sample with 1.2-μm-tall Ge crystals in Fig. S1c. **b**, **c**, θ–2θ and ω scans around Ge(004) reflection. The blue arrow in (b) indicates the peak maximum. The ω scan in (c) was modelled by a sum of 3 Gaussians.

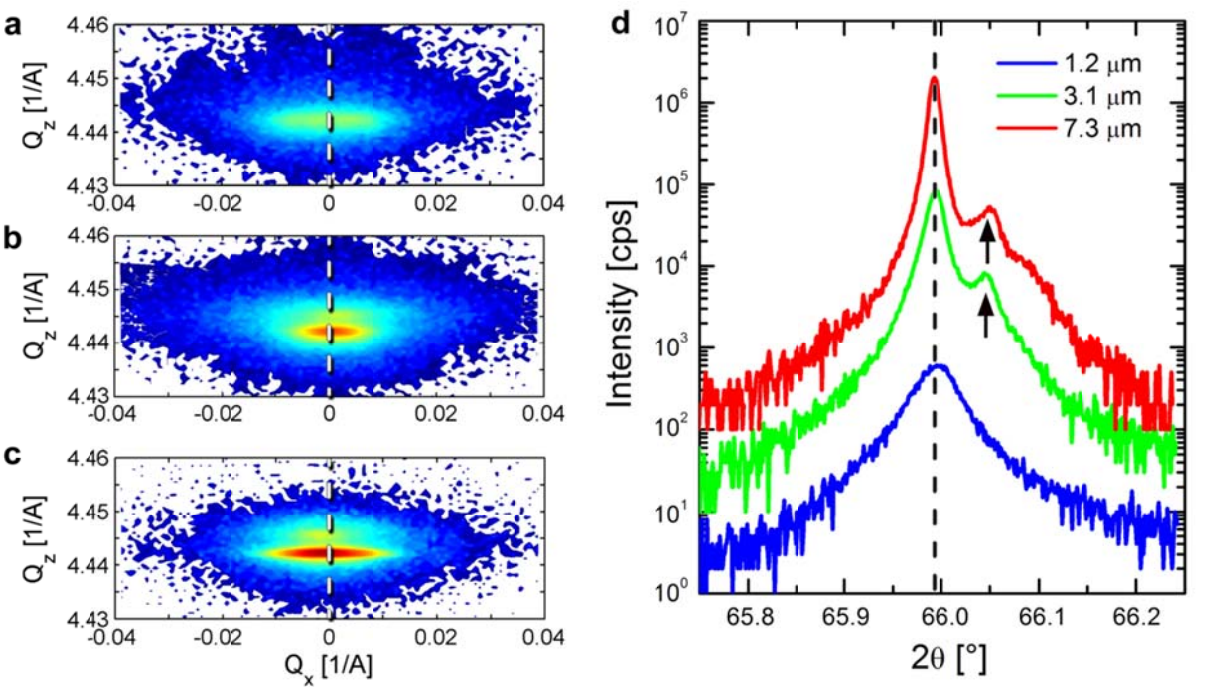

Figure S5 | RSMs measured around Ge(004) Bragg peak for sample with 1.2-μm (**a**), 3.1-μm (**b**) and 7.3-μm (**c**) tall Ge crystals in Fig. S1c–e. **d**, Corresponding θ–2θ scans around the Ge(004) reflection for the 3 samples. The position of relaxed Ge is indicated by the black dashed line. Contributions from the strained material in the trenches are indicated by black arrows. Scans for 3.1-μm and 7.3-μm-tall Ge crystals were multiplied by 10 and 100, respectively.

In addition, a modulation with a corresponding periodicity $d_{[001]} = \lambda/(2\Delta\omega_z \cos\theta) \sim 246$ nm is observed along the Q_z direction ($\Delta\omega_z$ is the angle between two adjacent satellite peaks along the Q_z direction)[37], stemming from the periodic arrangement of ripples formed on the Si pillar side walls during the DRIE process (period from SEM ~ 260 nm; Figs. S1b, S3b). The coherence between the Si pillars is, however, destroyed for Ge coverage as low as 1.2 μm (Fig. S3c). This suggests that strain imposed by the Ge induces minute random tilts between the Si pillars. The θ –2θ and ω scans around the Ge(004) reflection show that the Ge crystals are just very slightly strained (~ 0.008%) (Fig. S4b), and there is a significant lattice tilt indicated by two components with full-width-at-half-maximum (FWHM) of ~ 0.111° displaced by ~ ±0.054° along the [110] direction (Fig. S4c). Moreover, with the increase of the deposited thickness the width of the θ – 2θ scan decreases (Fig. S5). This indicates that the number of threading dislocations decreases with increasing height. Besides the main signal attributed to the relaxed epitaxial Ge material deposited on the Si pillars, weak contributions are observed towards larger 2θ angles, stemming from the tensile-strained material deposited in the deep trenches.

S3. Synchrotron scanning X-ray nanodiffraction

S3-A. Three-dimensional reciprocal space maps and their projections

In order to map the strain status locally, we performed X-ray experiments at the ID01 beamline of the European Synchrotron Radiation Facility (ESRF), using an 11.07 keV beam focused down to ~ 300×500 nm by means of Fresnel zone plates (FZP) and a Huber diffractometer equipped with

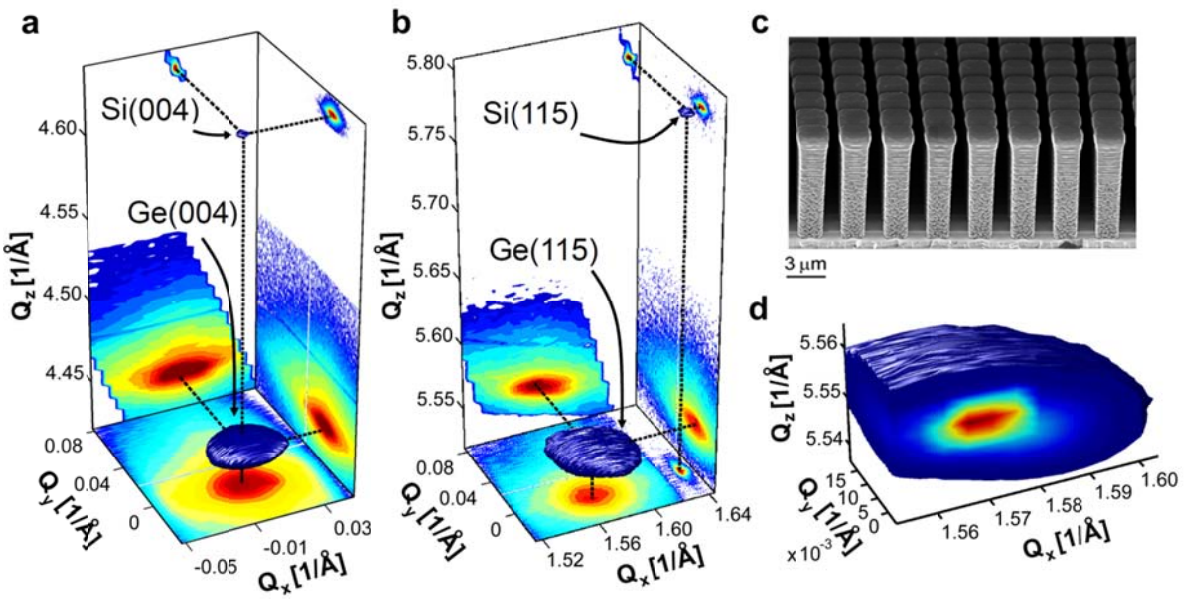

Figure S6 | 3D RSMs around Si and Ge recorded in the middle of one of the 1.2-μm-tall Ge crystals in (**c**) for (004) (**a**) and (115) (**b**) scattering geometries. **c**, Perspective-view SEM micrograph of an array of 1.2-μm-tall Ge crystals grown on patterned Si wafers with 8-μm-tall and 2-μm-wide Si pillars, spaced by 1 μm. **d**, Cut through the Ge(115) peak in (b) at $Q_y = -0.004$ Å^{-1} and $Q_x = 1.552$ Å^{-1}.

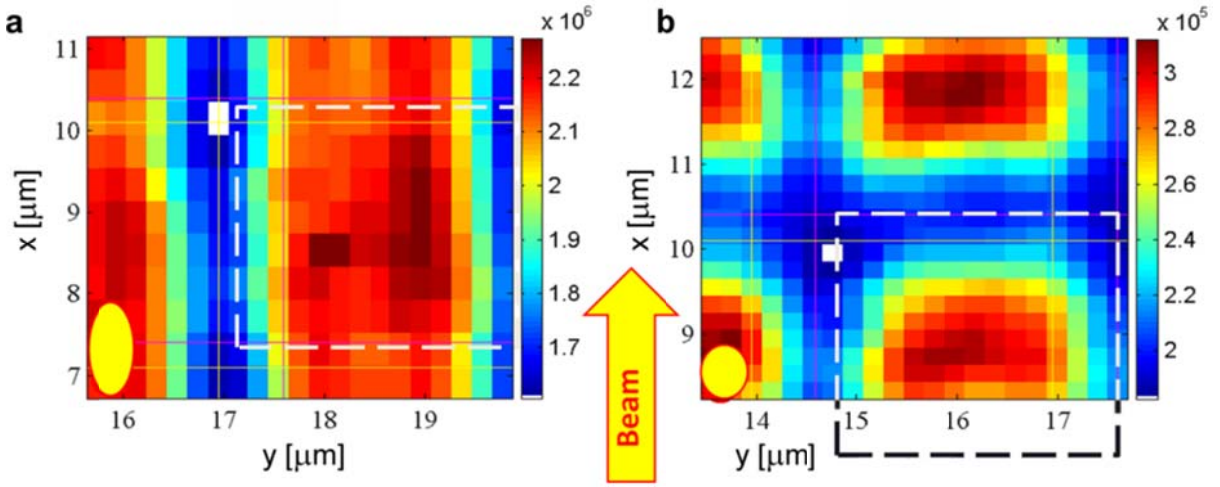

Figure S7 | Total intensity (x,y) plots for four 1.2-μm-tall Ge crystals, measured in the (004) (**a**) and (115) (**b**) scattering geometries. The shape of the beam is indicated in the lower left in both cases. The dashed rectangle indicates the location of one Ge crystal.

a high-precision (x,y,z) piezo-stage. For symmetric (004) and asymmetric (115) reflections, the incidence angle ω of the X-ray beam was scanned while moving the beam across the sample. Such an extremely small beam allowed us to scan the individual pillars and to record the scattered intensity in the plane parallel to the sample surface. Since a 2D pixel detector was used, three-dimensional (3D) RSMs could be constructed for each (x,y) position of the X-ray beam on the sample. 3D RSMs were built from rocking scans, varying the incidence angle ω of the primary focused beam. Example of such 3D RSMs around (004) and (115) Bragg peaks for both Si and Ge, recorded in the middle of a 1.2-μm-tall Ge crystal, are shown in Fig. S6. Together with the 3D reflections, plotted at a fixed iso-intensity level, the projected total intensities along Q_x, Q_y and Q_z are also shown. As an example, the projected (Q_x,Q_z) intensity map contains the intensity summed over the Q_y direction at each reciprocal space point (Q_x,Q_z).

S3-B. Spatial resolution

The FZP creates a beam spot which is slightly elliptical, with a width of 500 nm in the y-direction (perpendicular to the scattering plane), and 300 nm in the z-direction (perpendicular to the sample stage for zero incidence angle). Depending on the scattering geometry, e.g. incidence and exit angle, the projected beam spot on the sample becomes elongated in the x-direction, along the beam. This effect is of course much more pronounced for low incidence angles ω than for high incidence angles. Thus, measurements in the (115) scattering geometry are expected to be more precise than those measured around (004). Indeed, for the (004) reflection the incidence angle is ~ 24°, and the width of the beam spot along the x-direction of the sample is ~ 740 nm. For the (115) reflection the corresponding numbers are ~ 47° and ~ 410 nm, respectively.

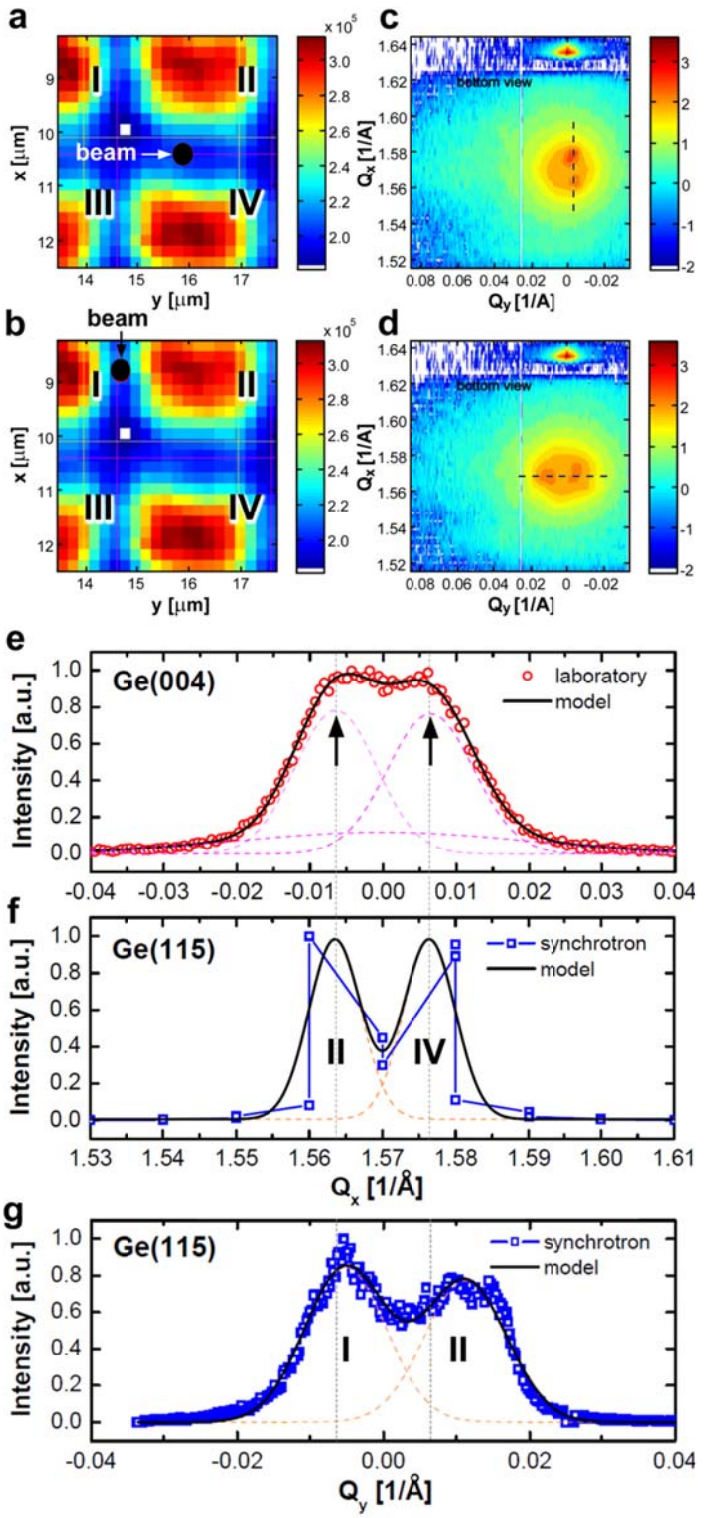

Figure S8 | a, **b**, Total intensity (x,y) plots for four 1.2-μm-tall Ge crystals. (Q_x,Q_y) projection of the 3D RSM for Ge(115) re-flection, measured when the X-ray beam is in the middle of the horizontal trench (**c**) and middle of the vertical trench (**d**). **e**, Cross-section along Q_x through the (Q_x,Q_z) RSM measured by laboratory HRXRD. Cross-sections along Q_x (**f**) and along Q_y (**g**) through the maxima of the (Q_x,Q_y) projections in (**c**) and (**d**).

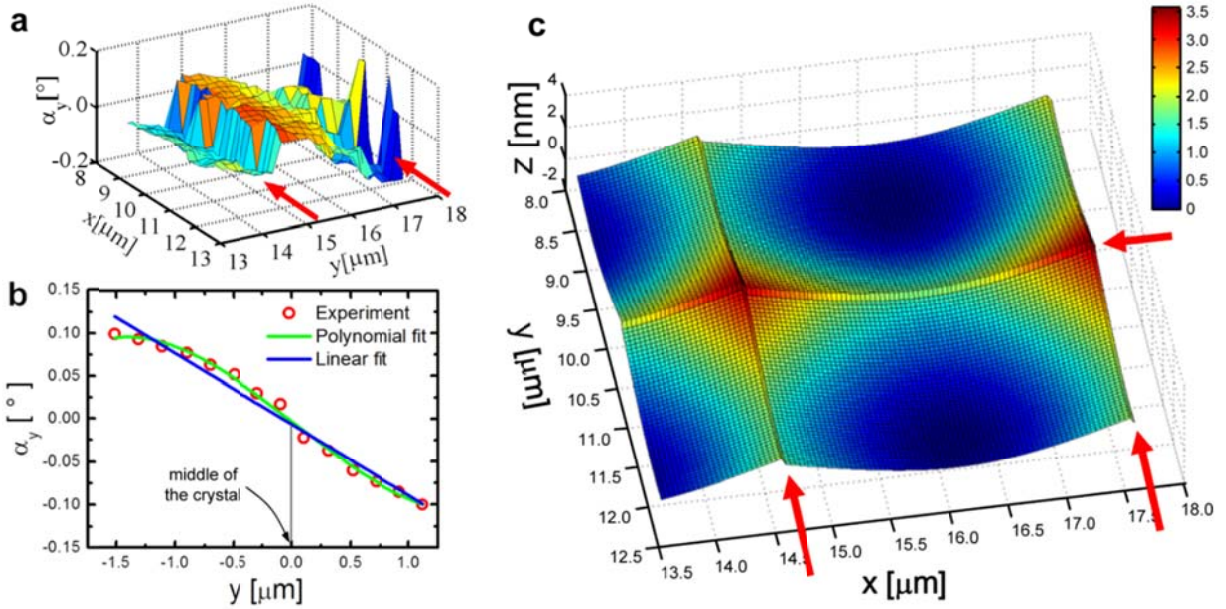

Figure S9 | a, Tilt along the Q_y direction (α_y) in the (x,y) plane determined from the Ge(004) reflection . **b**, Tilt along the Q_y direction averaged over the x-direction. **c**, Crystal lattice envelope for the 1.2-μm-tall Ge crystals in Figs. S1c and S6c. Red arrows in (a) and (c) indicate the trench positions.

Along the y-direction perpendicular to the scattering plane, the beam size remains on the other hand the same for all incidence angles. As a result, the trenches can be resolved both in the x- and y-directions for the (115) reflection as shown in Fig. S7b, whereas for the (004) reflection the resolution along x is lost (Fig. S7a). Unfortunately, in view of geometrical limitations (e.g. FZP and optical microscope mounted close to the sample), symmetrical reflections with steeper incidence angle could not be accessed in order to increase the resolution along x. Interestingly, when the X-ray beam hits the trench midway between two Ge crystals, the (Q_x,Q_y) projection exhibits two local maxima at approximately the same position as those measured by laboratory HRXRD (Figs. S4c, S8e–g). As we shall see these maxima are due to bowing of (001) lattice planes, causing them to be tilted in opposite directions close to the perimeter of neighbouring crystals.

S3-C. Measurement of lattice bending

As we have seen before, the laboratory HRXRD experiments indicate that even the shortest Ge crystals are fully relaxed. This applies both to misfit and thermal strain. The question still to be answered is how the strain relaxation comes about at a microscopic scale. The 3D RSMs measured around symmetric and asymmetric reflections allow us to determine the strain status of the layers. Before explaining our method, let us briefly discuss the common procedure to determine tilt and strain, based on information contained in the (Q_x,Q_z) scattering plane. The lattice tilt is first determined from an RSM measured around a symmetric reflection. Subsequently, the strain is extracted from an asymmetric reflection after its correction for the tilt.

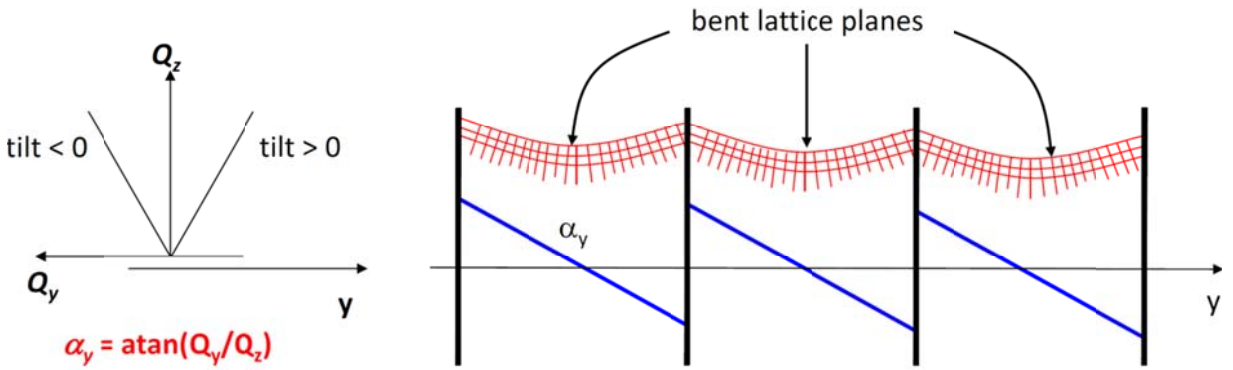

Figure S10 | Due to the bent lattice planes, the tilt α_y exhibits a "sawtooth" dependence on y.

In order for this procedure to be adopted in our nanodiffraction setup, the signals from symmetrical and asymmetrical reflections obviously have to be collected from the same sample area. Now we have shown before (Fig. S7b) that the Ge crystals can easily be identified by monitoring the scattered intensity of a (115) reflection while scanning the sample in the (x,y) plane. There are indications, however, that upon changing the incidence angle for the symmetric (004) reflection the beam spot may move across the sample by a few microns along the x-direction. Since along that x-direction the Ge crystals for the (004) scattering geometry cannot be resolved (see Fig. S7a), we cannot guarantee to remain at the previously defined position. This precludes meaningful tilt and strain measurements at well defined (x,y) positions by means of the standard procedure outlined above. Fortunately, the peak position along the Q_y direction normal to the scattering plane is not influenced by strain both for (004) and (115) geometries. The local crystal tilts perpendicular to the scattering plane can hence be determined by the expression $\alpha_y = arctan(Q_y/Q_z)$. Assuming the Ge crystals to have four-fold symmetry, it is sufficient to determine the tilt α_y. In order to obtain the variation of the local lattice tilt within an individual crystal, we determine the peak position (Q_y), at every point (x,y). We find that in a first approximation Q_y depends linearly on y across a single crystal (Fig. S9a, b), and in a "sawtooth" manner along rows of crystals (Fig. S10). The approximately periodical "sawtooth" function corresponds to the periodicity of the substrate pattern. In the x-direction only a small random change of this dependence is found. The observed linear change of the local tilt α_y with y corresponds to a spherical bending of the (001) lattice planes with a radius of curvature $R=[(1/Q_z)(dQ_y/dy)]^{-1}$. This is in fact the reciprocal value of the derivative of tilt with respect to y (see the crystal lattice envelope function in Fig. S9c). The random variations of α_y (Fig. S9a) can be mostly attributed to lattice variations due to crystal defects close to the Ge–Si interface, such as strain fields from misfit dislocations.

S4. Three-dimensional FEM calculations

Lattice bending and strain parameters obtained from scanning nanodiffraction data were compared with simulations based on Finite Element Method (FEM), which were performed using the

finite element analysis software package COMSOL Multiphysics. The simulated 3D geometries were built based on top- and cross-sectional SEM images. The numerical calculations were performed by meshing these geometries with 218550 and 302087 elements for 1.2 and 3.1-μm-tall Ge crystals, respectively. An initial hydrostatic expansion in the Ge pillar was considered, which was equal to 0.20%, as derived from the difference in the thermal expansion coefficients of Si and Ge for a step in temperature of ~ 500°C[38]. The different lattice parameters of Ge and Si and thermal expansion result in lattice strain in the form of convex bowing. The calculations provided all 6 components of the displacement gradient tensor, J_{ij} ($i, j = x, y, z$), which were used to compute the displacement field $\mathbf{u} = (u_x,u_y,u_z)$ using boundary conditions and reference points $\mathbf{r_0}$[39]:

$$\mathbf{u}(\mathbf{r}) = \left(u_x, u_y, u_z\right) = \mathbf{u}(\mathbf{r_0}) + J \cdot \begin{bmatrix} x - x_0 \\ y - y_0 \\ z - z_0 \end{bmatrix}, \tag{1}$$

where the displacement gradient tensor J is expressed by:

$$J = \begin{bmatrix} \frac{\partial u_x}{\partial x} & \frac{\partial u_y}{\partial x} & \frac{\partial u_z}{\partial x} \\ \frac{\partial u_y}{\partial x} & \frac{\partial u_y}{\partial y} & \frac{\partial u_z}{\partial y} \\ \frac{\partial u_z}{\partial x} & \frac{\partial u_z}{\partial y} & \frac{\partial u_z}{\partial z} \end{bmatrix} = \varepsilon + \Omega\,. \tag{2}$$

In (6) ε and Ω represent the symmetric and antisymmetric (rotation) tensors, respectively:

$$\varepsilon = \begin{bmatrix} \frac{\partial u_x}{\partial x} & \frac{1}{2}\left(\frac{\partial u_y}{\partial x} + \frac{\partial u_x}{\partial y}\right) & \frac{1}{2}\left(\frac{\partial u_x}{\partial z} + \frac{\partial u_z}{\partial x}\right) \\ \frac{1}{2}\left(\frac{\partial u_y}{\partial x} + \frac{\partial u_x}{\partial y}\right) & \frac{\partial u_y}{\partial y} & \frac{1}{2}\left(\frac{\partial u_y}{\partial z} + \frac{\partial u_z}{\partial y}\right) \\ \frac{1}{2}\left(\frac{\partial u_x}{\partial z} + \frac{\partial u_z}{\partial x}\right) & \frac{1}{2}\left(\frac{\partial u_y}{\partial z} + \frac{\partial u_z}{\partial y}\right) & \frac{\partial u_z}{\partial z} \end{bmatrix}, \tag{3}$$

$$\Omega = \begin{bmatrix} 0 & \frac{1}{2}\left(\frac{\partial u_y}{\partial x} - \frac{\partial u_x}{\partial y}\right) & \frac{1}{2}\left(\frac{\partial u_x}{\partial z} - \frac{\partial u_z}{\partial x}\right) \\ -\frac{1}{2}\left(\frac{\partial u_y}{\partial x} - \frac{\partial u_x}{\partial y}\right) & 0 & \frac{1}{2}\left(\frac{\partial u_y}{\partial z} - \frac{\partial u_z}{\partial y}\right) \\ -\frac{1}{2}\left(\frac{\partial u_x}{\partial z} - \frac{\partial u_z}{\partial x}\right) & -\frac{1}{2}\left(\frac{\partial u_y}{\partial z} - \frac{\partial u_z}{\partial y}\right) & 0 \end{bmatrix} \tag{4}$$

The magnitude of displacement field $|\mathbf{u}|$ and three components of the strain tensor (ε_{xx},ε_{xz},ε_{zz}) in the median vertical plane of 1.2 and 3.1-μm-tall Ge crystals are plotted in Fig. S11. Zero displacement was defined at the SiGe boundary ($z = 0$). Since the Ge crystals shrink during the cooling process after growth, the highest total displacements are at the top of the crystals. To find the bending of crystal planes we calculate the asymmetrical tensor, since the components Ω_{ij} (x,y,z) represent the angles of rotation of the elementary unit cell. Ge crystals have fourfold symmetry, $\Omega_{xz} = \Omega_{yz}$, and therefore we need to calculate only the Ω_{yz} (x,y,z) components. These values represent small local rotation angles of lattice planes around the x-axis at the point (x,y,z).

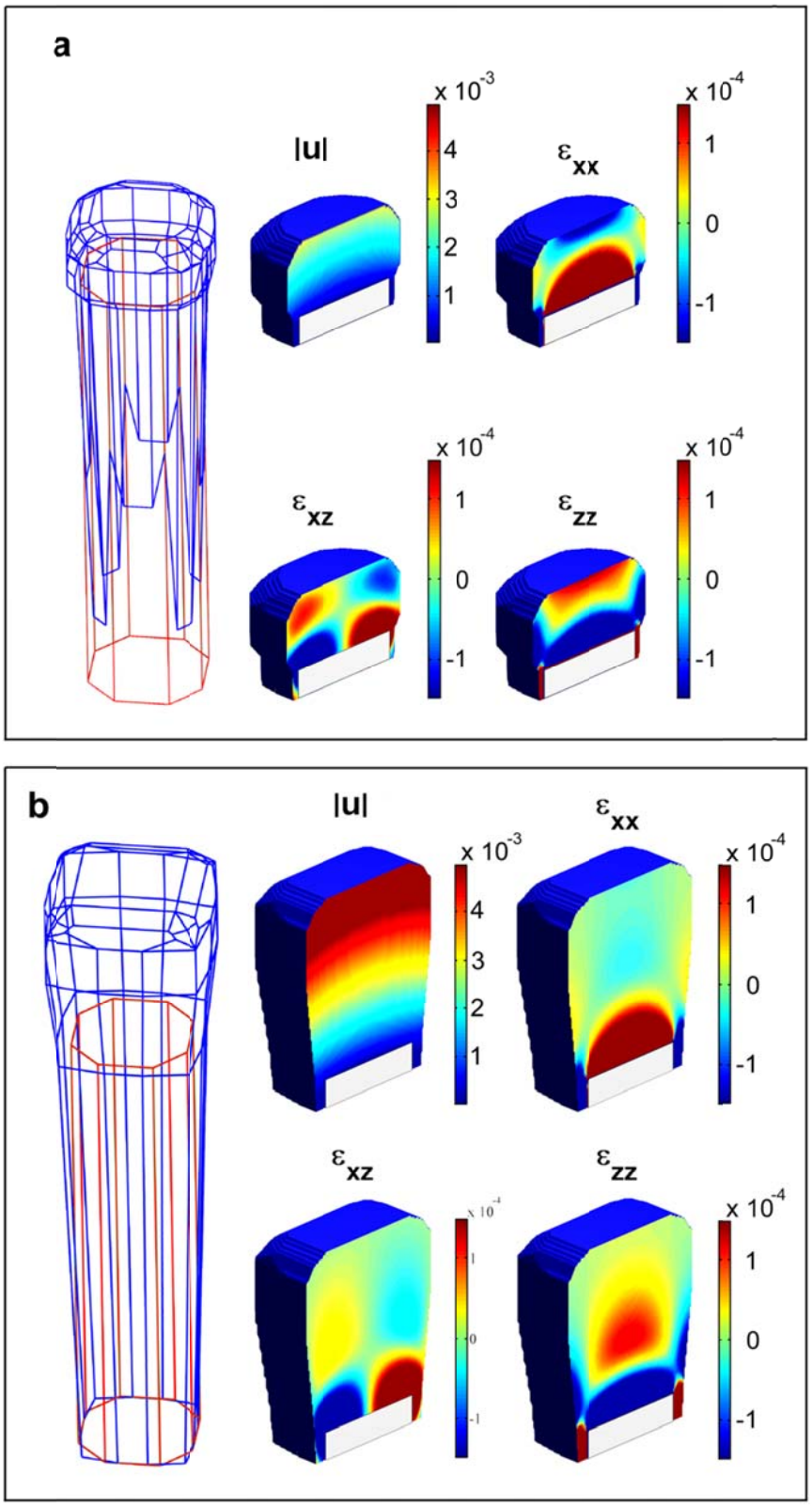

Figure S11 | Three-dimensional FEM calculations. a, 1.2-μm-tall Ge crystals; **b**, 3.1-μm-tall Ge crystals.

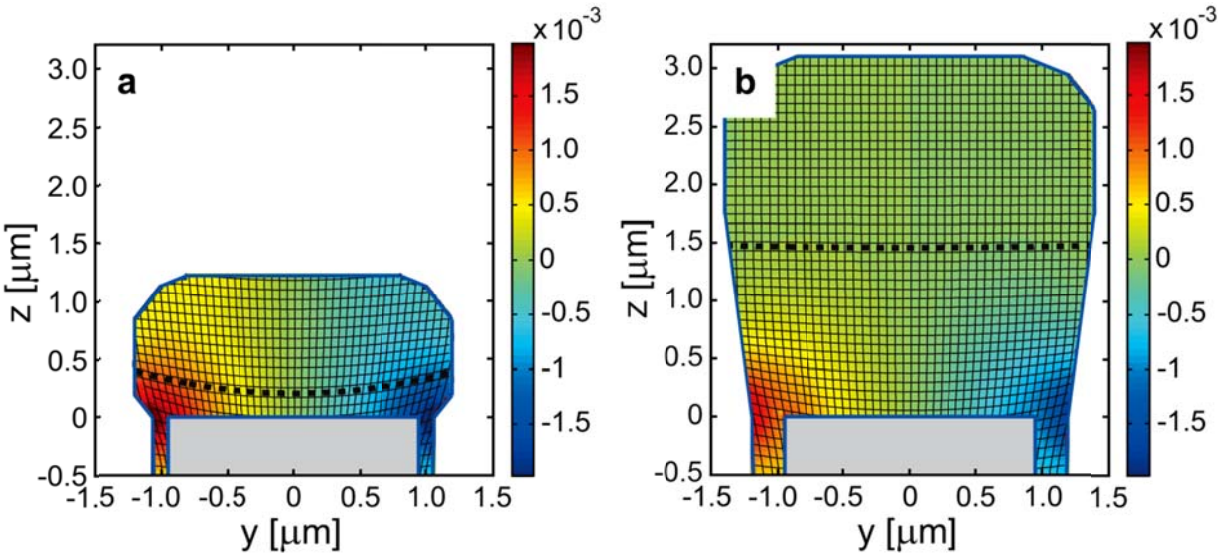

Figure S12 | Lattice bending extracted from the rotation tensor obtained from FEM calculations for: 1.2-μm (**a**) and 3.1-μm (**b**) tall Ge crystals. The color maps represent cross-sections through the *yz* component of the 3D rotation tensor sliced in the middle of the Ge crystals ($x = 0$). The thick dashed black lines represent the experimental curvatures obtained from synchrotron submicron diffraction experiments. The position of the experimental curve along the *z*-axis was chosen such that it matches the curvature calculated by FEM. The scale of the lattice bending was scaled by a factor of 200 to enhance the visibility of local strain.

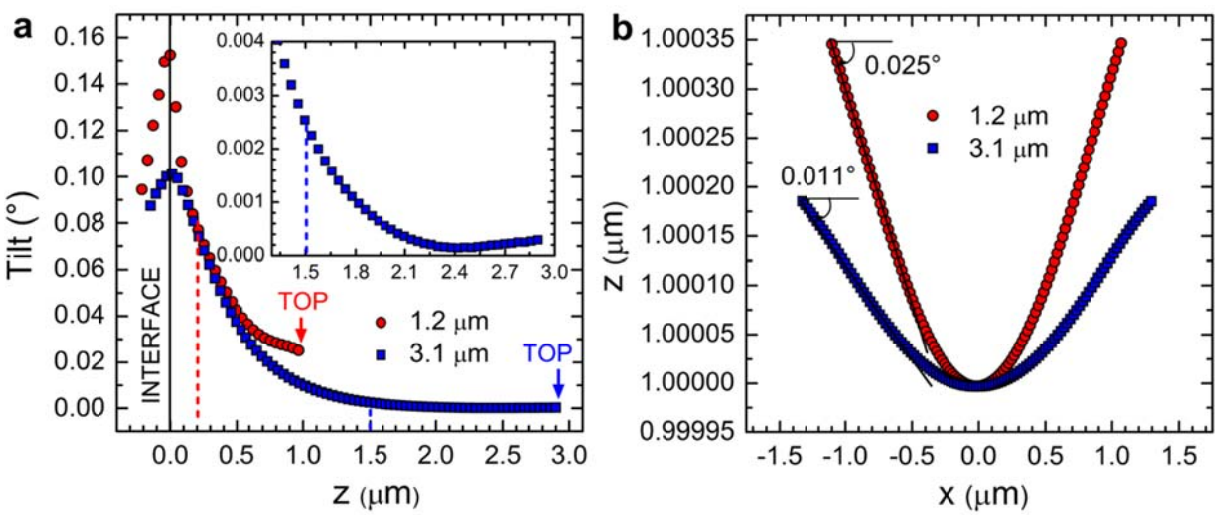

Figure S13 | a, Tilt of the lattice planes at the crystal sidewalls as obtained from FEM calculations (y = 1.05 μm and y = 1.18 μm for 1.2 and 3.1-μm-tall crystals, respectively). The inset shows an enlarged section of the tilt vs. *z* dependence for the 3.1-μm-tall crystal. The dashed straight lines in red and blue indicate the positions along the crystal height where the lattice bending from FEM calculations matches the results obtained from scanning X-ray nanodiffraction. **b**, Curved lattice planes at a height z = 1 μm for 1.2 and 3.1-μm-tall crystals.

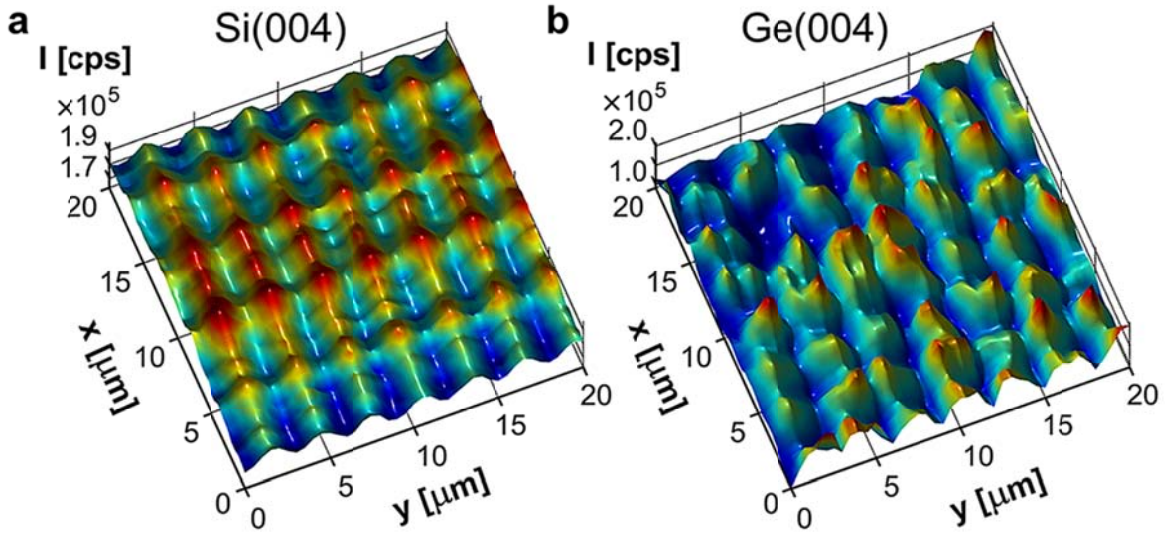

Figure S14 | Position sensitive intensity maps recorded at fixed incidence angles for Si(004) (**a**) and Ge(004) (**b**) reflections, corresponding to sample in Figs. S1c, S6c.

The lattice bending in the (y,z) plane was obtained by integrating for any z position, $\Delta z(y) = \int \Omega_{yz}(x,y,z)dy$ (Fig. S12). Figure S13 shows how the tilt of the lattice planes at the edge of the crystal, corresponding to lattice bending, quickly decays with the crystal height. Thus, for a 3.1-μm-tall Ge crystal the tilt at the sidewalls near the interface is ~ 0.1° and at a height of 2.4 μm has already dropped to ~ 0.0001°.

S5. Assessment of net tilts

In the last section we have shown that there is a local tilt of (001) lattice planes within each Ge crystal due to bowing of these planes. In addition there is a net or average tilt of every crystal as a whole. This net tilt can be visualized qualitatively as follows. Imagine first that normal to the sample to be aligned with the scattering plane for the Si(004) reflection of the substrate in the unpatterned region. The intensity of the Si(004) is then recorded at different (x,y) positions in the patterned area (see Fig. S14a). We do the same for Ge(004) reflection after adjusting the incidence angle. First of all, we observe that both the Si pillars below and Ge crystals above are nicely resolved (Fig. S14). Second, we see that the (x,y) position sensitive XRD intensity map of the Si(004) reflection exhibits maxima arranged in the regular pattern of the underlying substrate, as expected for Si pillars being part of the substrate and at most being subject to an immeasurably small tilt (Fig. S14a). On the other hand, the corresponding map for the Ge(004) reflection exhibits maxima displaced from the Si(004) maxima in a random manner (Fig. S14b). This proves that the Ge crystals are randomly tilted with respect to the Si pillars. For a quantitative evaluation of the net tilt we have to separate Ge crystals into two classes, (a) short crystals in which local tilts due to bowing dominate, and (b) tall crystals in which bowing is negligible apart from a region close to the interface.

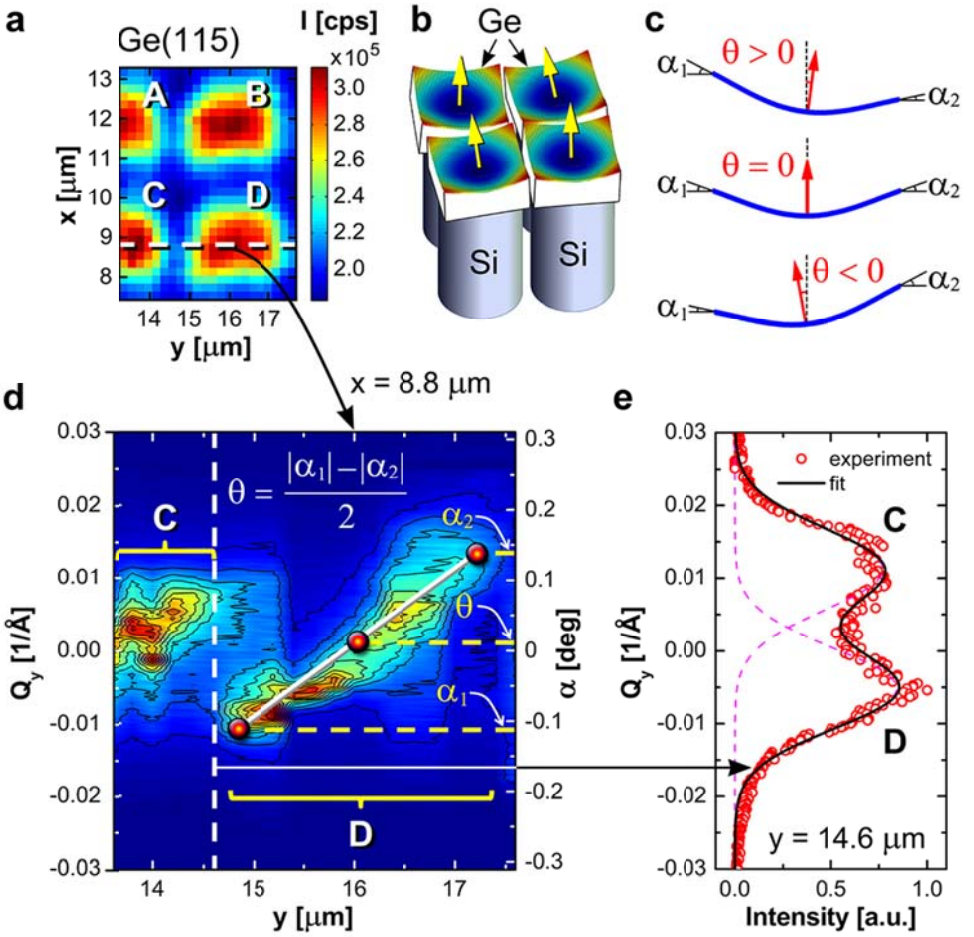

Figure S15 | Assessment of net tilts for short Ge crystals. a, Total intensity (x,y) map for Ge(115) reflection recorded in the area of four 1.2-μm-tall Ge crystals (A, B, C and D). **b**, Schematic of four short Ge crystals with different net tilts. **c**, Calculation of the net tilt (θ) from asymmetry of the lattice bending. The angles α_1 and α_2 are the tilts at the side walls of a crystal. **d**, (y,Q_y) contour plot corresponding to x = 8.8 μm (i.e. line traversing the lower row of pillars through their middle). The dashed white line indicates the position of the vertical trench. **e**, Cross-section through the (y,Q_y) contour plot in (d) at y = 14.6 μm. The two maxima correspond to tilted lattice planes in crystals C and D, respectively.

S5-A. Short crystals

For short Ge crystals (e.g. 1.2 and 3.1 μm) we can determine the net tilt from asymmetry of the bending as schematically shown in Fig. S15b, c. A plot of the intensity maximum of the Ge(115) peak in the (Q_x,Q_y) plane (see Fig. S8d) versus the y coordinate gives us the dependence of the tilt angle (α) on y. An example of such a plot for fixed x = 8.8 μm, corresponding to the line traversing the middle of pillars C and D in Fig. S15a, is shown in Fig. S15d. We observe again the typical "sawtooth" dependence of Fig. S10. Now this plot not only gives the curvature radius of the lattice planes for a given crystal at a certain position x, but also allows us to find the net tilt θ by averaging the tilt angles at the perimeter of the crystal, α_1 and α_2, as shown schematically in Fig. S15c.

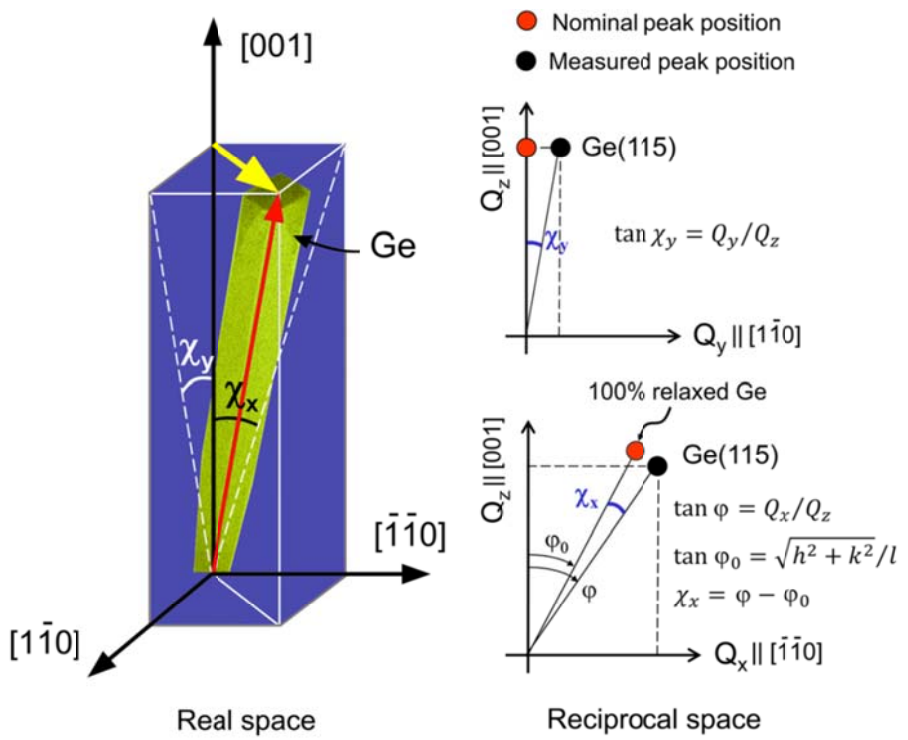

Figure S16 | Assessment of net tilts for tall Ge crystals. Schematic showing how the net tilt between the symmetry axis of a tall Ge crystal (red arrow) and the [001] direction is determined. The yellow arrow is the displacement vector and its magnitude is exaggerated to enhance the visibility of local tilt, which is of the order of ~ 0.1°.

By averaging now over the *x* coordinate for each of the 4 crystals in Fig. S15a, we obtain net tilts below 0.02°. This is much smaller than the maximum tilt of ~ 0.1° at the perimeter of the Ge crystals, which, as we have seen, stems from the bowing of (001) lattice planes.

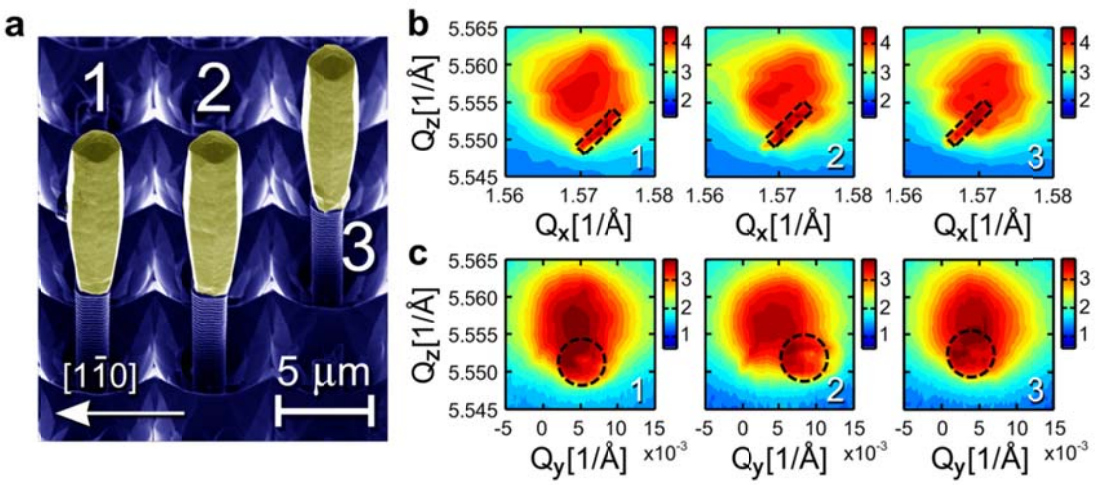

Figure S17 | a, SEM micrograph of three isolated 11-µm-tall Ge crystals. Projections of the 3D RSMs along Q_y (**b**) and Q_x (**c**) directions, measured at the top of the three crystals in (a). The dashed rectangles and circles indicate the diffraction peak stemming from the Ge crystal.

S5-B. Tall crystals

For tall Ge crystals we determine the net tilt by measuring the deviations of the peak position from the nominal value (i.e. 100% relaxed Ge with no tilt) in the (Q_x,Q_z) and (Q_y,Q_z) planes by using the following formulas (see Fig. S16):

$$\tan \chi_y = Q_y/Q_z, \quad (5)$$

$$\chi_x = \varphi - \varphi_0, \quad (6)$$

$$\tan \varphi = Q_x/Q_z, \quad (7)$$

$$\tan \varphi_0 = \sqrt{h^2 + k^2}/l. \quad (8)$$

For isolated Ge crystals we measured the net tilt at different positions along their height. Since the thickness of the crystal is still comparatively small with respect to the penetration depth of X-rays in Ge, the X-rays practically shine through. Hence, the sharp peak stemming from the tall Ge crystal is superimposed on a weaker broad peak attributed to the tensile-strained material in the trenches (Figs. S17b, c). We repeated this procedure for the three Ge crystals depicted in Fig. S17a. Since the position of the sharp peak in the (Q_x,Q_z) and (Q_y,Q_z) planes changes from crystal to crystal (Fig. S17b, c), each crystal has its own distinct net tilt.

S6. Resolution function

The instrumental resolution function in reciprocal space mapping is determined by the resolution area A_E. This is a measure of the angular space illuminated by the incident beam and of the angular acceptance of the detector, whose shape depends on the position in reciprocal space[40]. In case of using a pixel detector one of the limiting factors is the pixel size which in our case was ~ $\Delta\theta_e$ = 0.003 °/pixel (10” per pixel).

The second limiting factor is the beam divergence. The beam focused by a Fresnel zone plate exhibits quite a large divergence due to geometrical limitations of the experimental set up (Fig. S18a). The investigated sample is irradiated by a conically shaped beam focused onto the sample. The scattered beam defocuses, and the response on the pixel detector is visible as a disc (see Fig. S18b). The angular size of the disc on the pixel detector defines the beam divergence and thus the resolution within the incidence angle for both in-plane (e.g. Q_x, Q_z) and out-of-plane (Q_y) directions. The angular diameter of the disc was $\Delta\theta_i$ = 0.08° in our experiment. Basically, the beam divergence $\Delta\theta_i$ and the detector resolution $\Delta\theta_e$ define a 3D window in reciprocal space, which has the shape of a disc with diameter ~ $K{\cdot}\Delta\theta_i = 8{\times}10^{-3}$ Å^{-1} and height $\Delta K{\cdot}\Delta\theta_e = 4{\times}10^{-4}$ Å^{-1}, where K is the modulus of the scattering vector. This disk is oriented perpendicular to the incident beam, as shown in Fig. S18c. The measured signal is then a convolution of the window function with the scattered intensity.

However, since the resolution in the RSM is also limited by the measurement step, the real dimensions of the resolution window depicted in Fig. S18d by a rectangular box are $8{\times}10^{-3}$ Å^{-1} and $1{\times}10^{-3}$ Å^{-1}, respectively.

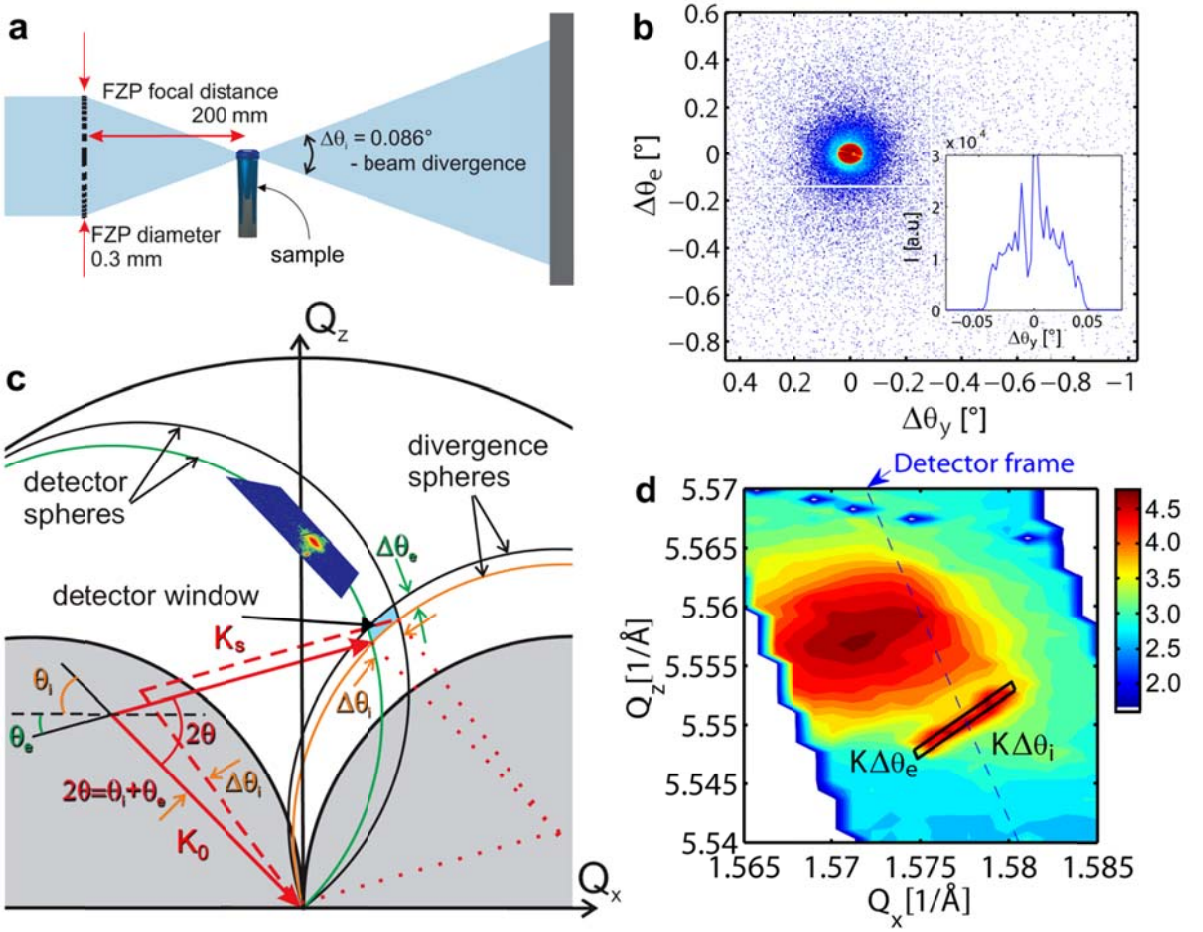

Figure S18 | Resolution function. a, Principle of beam focusing by a Fresnel zone plate (FZP). A FZP with the diameter of 0.3 mm, placed at ~ 200 mm from the sample, focuses the beam down to ~ 300 nm. The beam defocuses after the sample and is recorded by a detector. **b**, Overfocused primary beam as measured by the pixel detector. **c**, Ewald construction in the (Q_x,Q_z) plane. The incident beam (vector K_0, incidence angle θ_i, divergence $\Delta\theta_i$) and the exit beam (vector K_s, exit angle θ_e, detector resolution $\Delta\theta_e$) define a window in reciprocal space, which is the resolution function. The detector and divergence spheres (diameter $2K$, $K = |K_0| = |K_s|$) are defined by reciprocal points for which θ_i is fixed and θ_e changes from 0 to 360°, and vice-versa, respectively. The grey areas define the inaccessible regions for Bragg geometry, when either the beam or the detector is behind the sample (*Note:* these regions are accessible for Laue geometry). The upper sphere with diameter $4K$ represents the limiting sphere, and defines the accessible region for a given X-ray wavelength. **d**, (Q_x,Q_z) projection of the 3D RSM measured for an isolated Ge single crystal which was irradiated by the nanofocused beam. The rhomboidal box with sides $K\Delta\theta_i$ and $K\Delta\theta_e$ depicts the resolution function in the (Q_x,Q_z) plane. Two diffraction peaks are observed, a sharp one stemming from the Ge crystal grown on top of the Si pillar, and a broad, weak one, due to the tensile strained material in the trenches.

The diffracted signal from the Si substrate in the Bragg geometry has the form of a truncation rod perpendicular to the sample surface for a plane wave. The rod width corresponds to the width of the Darwin curve[41], which for a Si(115) reflection and X-ray energy of 11keV is ~ 0.7’’

($\Delta Q_z = 6\times10^{-5}$ Å^{-1}). The width of the dynamical diffraction curve for a Ge crystal has to be considered in the Laue geometry since the crystal is irradiated through its sidewalls. The width of the Laue diffraction curve for a Ge(115) reflection for a plane wave at 11 keV is ~ 10'' ($\Delta Q_x = 4\times10^{-4}$ Å^{-1}) for a crystal with the thickness of ~ 1.5 μm. Since the extinction length in the Laue geometry for Ge(115) is ~ 25 μm, much larger than the crystal size, the diffraction can be considered as kinematical and therefore $\Delta Q_x = 2\pi/(1.5\ \mu m) = 4\times10^{-4}$ Å^{-1}. If we now compare the size of our disc-shaped resolution function with the theoretical widths of diffraction curves, it is clear that the resolution function will dominate even if the scattered signal comes from a perfect crystal. Such a situation was observed also in our RSMs where the Si substrate peak has disc shape. Similarly, the diffraction signal stemming from the Ge crystal exhibits a shape in the form of a thin disc, overlapped with a broad, weak signal from Ge deposited in the trenches, see Fig. S18d. The cross-sections along the Q_x and Q_z directions through the (115) peak stemming from the Ge crystal have FWHM ~ 1×10^{-3} Å^{-1}. Similar values are also obtained for the Si peak. The theoretical peak width for Ge (along Q_x due to high aspect ratio) is only slightly smaller than the height of the window disc. Since the disc height in reciprocal space is almost equal to the theoretical diffraction width of a defect-free crystal, this proves that defects do not contribute to the diffraction signal in our RSMs. The Ge crystals can therefore be considered defect free.

Supplementary references

[37] Pietsch, U., Holý, V. & Baumbach T. *High-resolution X-ray scattering: From thin films to lateral nanostructures*. New York: Springer, pp. 299-300 (2004).

[38] Slack, G.A. & Bartram, S.F. Thermal expansion of some diamond-like crystals. *J. Appl. Phys.* **46**, 89-98 (1975).

[39] Sokolnikov, I.S. *Mathematical theory of elasticity*, McGraw Hill Book Company, pp. 20-21 (1956).

[40] Pietsch, U., Holý, V. & Baumbach T. *High-resolution X-ray scattering: From thin films to lateral nanostructures*. New York: Springer, pp. 51-53 (2004).

[41] Bowen, D. K., Tanner, B. K. *High resolution X-Ray diffractometry and topography*. Taylor & Francis, pp. 101-103 (1998).

Supplementary movie legends

Supplementary movie 1 | Evolution of the 3D reciprocal space map (RSM) around Si(115) and Ge(115) Bragg reflections (e.g. projections (Q_x,Q_z) - upper left corner, (Q_y,Q_x) - upper right corner, and (Q_y,Q_z) - lower left corner) during scanning a nanofocused X-ray beam across an array of four 1.2-μm-tall Ge crystals (corresponding to Fig. 1a and d). The contour plot in the lower right corner represents the total scattered intensity from four crystals around the Ge(115) peak for all incidence angles. Steps along the *x*- and *y*-directions ("pix", "piy") are 400 and 200 nm, respectively. At each position a 3D RSM is built from a collection of 2D detector images obtained by rocking the incidence angle.

Supplementary movie 2 | Evolution of the 3D RSM around the Ge(115) reflection as a nanofocused X-ray beam explores the array of four 1.2-μm-tall Ge crystals of Fig. 1a and d. The 3D RSM is cut perpendicular to the *Qx* and *Qy* directions in order to reveal its internal structure.

Supplementary movie 3 | Similar to Supplementary Movie 1, but for an array of four 3.1-μm-tall Ge crystals (corresponding to Fig. 1b and e).

Supplementary movie 4 | Similar to Supplementary Movie 2, but for an array of four 3.1-μm-tall Ge crystals (corresponding to Fig. 1b and e).

Supplementary movie 5 | In order to probe the crystalline properties of a single Ge crystal by scanning X-ray nanodiffraction, neighbour crystals are removed inside a scanning electron microscope (SEM) by micro-macromanipulators that are driven by high-precision (*x*,*y*,*z*) piezo-stages. The movie shows the removal of a 11-μm-tall Ge crystal inside a scanning electron microscope by a micromanipulator. The field of view is ~ 30×32 μm.

Supplementary movie 6 | Evolution of the 3D reciprocal space map (RSM) around Ge(115) Bragg reflection (e.g. projections (Q_x,Q_z) - upper left corner, (Q_y,Q_x) - upper right corner, and (Q_y,Q_z) - lower left corner) during scanning a nanofocused X-ray beam across the 11-μm-tall Ge crystal (corresponding to Fig. 3a).

Supplementary movie 7 | Evolution of the 3D RSM around the Ge(115) reflection as a nanofocused X-ray beam scans the 11-μm-tall Ge crystal of Fig. 3a. The 3D RSM is cut perpendicular to the *Qy* direction in order to reveal its internal structure.